

See discussions, stats, and author profiles for this publication at: <https://www.researchgate.net/publication/231648500>

First-Principles Based Analysis of the Electrocatalytic Activity of the Unreconstructed Pt(100) Surface for Oxygen Reduction Reaction

ARTICLE *in* THE JOURNAL OF PHYSICAL CHEMISTRY C · MARCH 2012

Impact Factor: 4.77 · DOI: 10.1021/jp2075379

CITATIONS

18

READS

33

3 AUTHORS, INCLUDING:



Byungchan Han

Yonsei University

37 PUBLICATIONS 506 CITATIONS

[SEE PROFILE](#)



Venkatasubramanian Viswanathan

Carnegie Mellon University

35 PUBLICATIONS 984 CITATIONS

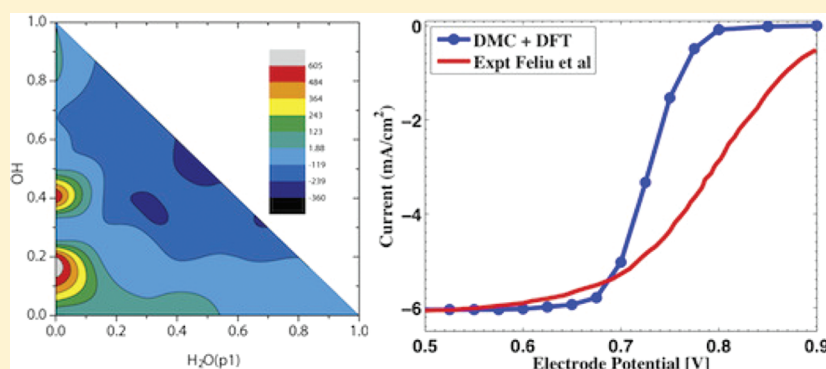
[SEE PROFILE](#)

First-Principles Based Analysis of the Electrocatalytic Activity of the Unreconstructed Pt(100) Surface for Oxygen Reduction Reaction

Byungchan Han,*† Venkatasubramanian Viswanathan,‡ and Heinz Pitsch*,‡

†Department of Energy Systems Engineering, DGIST, Daegu, 711-873, Republic of Korea

‡Department of Mechanical Engineering, Stanford University, Stanford, California 94305, United States



ABSTRACT: We apply a rigorous computational procedure combining ab initio DFT calculations and statistical mechanics based methods to examine the electrocatalytic activity of the unreconstructed Pt(100) surface for oxygen reduction reaction. Using the cluster expansion formalism, we obtain stable interfacial water structures using Monte Carlo simulations carried out using parametrized interactions of water–water and water–metal. We find that both long-range and multibody interactions are important to describe the adsorbate interactions as a consequence of the mismatch between the preferred “hexagonal” water overlayer and the underlying square symmetry of the (100) surface. Our results indicate that the stable interfacial water structure is substantially different from that found on the Pt(111) surface. We compute the potential-dependent equilibrium coverages of oxygen-containing adsorbates, which shows that the surface is poisoned by strongly adsorbed OH. We construct the free-energy diagram of intermediates for oxygen reduction reaction on the Pt(100) surface and find that the limiting step is the reduction of the strongly adsorbed OH. We also find that, at a given potential, a higher degree of poisoning by OH is the reason unreconstructed (100) surfaces are catalytically less active than (111) surfaces. This study shows the importance of accurately capturing atomistic interactions beyond the nearest neighbor pairs.

INTRODUCTION

Water is the most abundant chemical species on earth and vital for sustaining electrochemical reactions of great importance in biology, catalysis, sensor devices, and other areas. As such, the atomistic-level understanding and control of the interactions between water molecules and material surfaces have been central research topics over the last several decades.^{1–3} However, the complicated nature of the interaction (i.e., hydrogen bondings among water molecules) and its peculiar dependency on experimental conditions (i.e., substrates, impurities, and intermediates, etc.) have delayed the conclusive identification of the water structures on metal surfaces.^{4–6} Furthermore, the interpretation of the water structures observed by a variety of experimental techniques is not straightforward because of the different kinds of perturbations involved with the imaging or spectroscopic processes. The molecular-level understanding of the interfacial water structure is crucial in low temperature fuel cells, as it is the first step toward developing alternative catalysts of cheaper material cost, higher efficiency, and electrochemical stability than the conventional Pt metal.^{7–11}

State-of-the-art fuel cell catalysts are nanoparticles shaped by (111) and (100) facets with a small atomic fraction of edges and steps. The catalytic activity of these particles is known to depend significantly on the atomistic morphology of the catalyst surfaces.¹² As such, it is scientifically and technologically of interest to accurately characterize interface water structures and ORR activities on both of the facets. Density functional theory (DFT) calculations have been used successfully to predict trends in the electrocatalytic activity of (111) surfaces.^{13,14} However, the mismatch between the square lattice symmetry of the metal surface in the (100) orientation and the hexagonal water-hydroxyl overlayers found on other surfaces has made it difficult to obtain a detailed description of the adsorbate structures to characterize the activity on (100) surfaces.

Here, we apply a systematic methodology beyond the simple nearest-neighbor interaction models to determine the

Received: August 5, 2011

Revised: February 16, 2012

Published: February 21, 2012



electrocatalytic activity of the unreconstructed Pt(100) surface for oxygen reduction reaction. We limit our study and analysis to the unreconstructed Pt(100)-(1 × 1) surface. Although it is well-known that (100) surfaces undergo hex-reconstruction when annealed,¹⁵ in electrochemical environments, in contact with electrolytes, the Pt(100)-hex surface, prepared either in UHV or by a flame annealing method, is lifted and becomes a (1 × 1) surface with a lot of defects.¹⁶ In addition, Pt nanoparticles are truncated by the unreconstructed (100) surface and these surfaces are typically not expected to undergo hex-reconstruction.¹⁷

In this study, we determine the thermodynamically stable water structure at the solid–liquid interface using DFT calculated potentials for the interaction between water and the metal surface. Using this as a model for the solid–liquid interface, we compute a free-energy diagram of the different intermediates for oxygen reduction reaction. Using this, we carry out dynamic Monte Carlo (DMC) simulations to determine the structure of the adsorbate layer at different potentials, thereby determining the electrocatalytic activity for oxygen reduction reaction. A similar approach has been used earlier to quantify O-containing adsorbates formed from the electrochemical discharge of water, which compared well with voltammetric experiments on the Pt(111) surface.^{18,19}

MODEL APPROACH

The simulation of the kinetics of the oxidation of water and oxygen reduction reaction is accomplished through a combination of equilibrium and dynamic Monte Carlo methods using kinetic and thermodynamic parameters calculated from DFT. The combination of Monte Carlo methods is used to carry out an efficient time-scale separation, where the fast processes are assumed to be in equilibrium and the slow kinetic steps are handled by the dynamic Monte Carlo method.

DFT Calculations. We have used a model system of a six-layer slab stacked in the (100) direction of an fcc metal to simulate a Pt(100) surface. We also imposed a periodic boundary condition with a vacuum region of 14 Å to preclude interactions between the slab and its images. To optimize the structures, all adsorbates and Pt atoms in the topmost four layers are fully relaxed, while the bottommost two layers are fixed to the positions of the relaxed clean Pt slab. To obtain total energies, first principles DFT computations were performed with the projector augmented wave (PAW) method describing interactions between ions and electrons²⁰ and generalized gradient approximation (GGA) to DFT by Perdew–Burke–Ernzerhof²¹ as implemented in VASP.²² The cutoff energy for a plane wave was 340 eV, and the Fermi level was smeared by 0.2 eV using the Methfessel–Paxton method with an order of 1.²³ A lattice constant for the (100) surface of 3.98 Å was obtained from the ab initio DFT calculated bulk Pt which is close to the experimental value of 3.92 Å.²⁴ Reciprocal space integrations were done using Γ-centered grids with 13 × 13 × 1 *k*-points for a 1 × 1 unit cell and proportionally smaller meshes for larger supercells.

DMC Method. The dynamic Monte Carlo method pioneered by Gillespie²⁵ enables the efficient solution of the time evolution and the dynamics of chemical systems by solving the Master equation in a stochastic sense. Several algorithms have been subsequently developed for simulating catalyst systems, and all DMC simulations in this paper use a particularly efficient variant of the variable step size method (VSSM), called VSSMb.^{26,27} A more detailed discussion of the method can be found elsewhere.^{26–29}

RESULTS AND DISCUSSION

In this section, we begin by studying the effect of electric field on the stability of the water molecules adsorbed on the Pt(100) surface. Using a cluster expansion formalism, we determine the thermodynamically stable water structures at the solid–liquid interface. Using these results, we construct a free-energy diagram of the intermediates involved in the oxygen reduction reaction. These are used to carry out analysis of the potential dependent coverage of O-containing adsorbates and finally to evaluate the electrochemical activity of the Pt(100) surface for oxygen reduction reaction.

Effect of Electric Field. It has been reported that an electric field existing at the electrical double layer influences the chemical stability and internal geometry of adsorbed water molecules.³⁰ We have investigated these effects using a model system simulating the Pt(100) surface, as depicted in Figure 1.

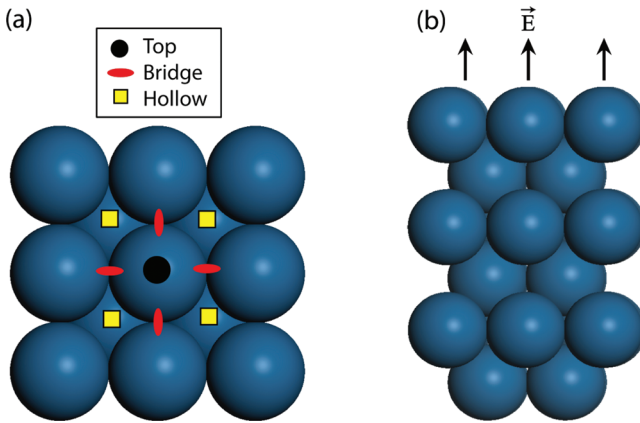


Figure 1. Schematic (a) top and (b) side views of the model system used for the Pt(100) surface. The adsorption sites for a water molecule and direction of applied electric field are indicated in the model system.

We have applied an external electrostatic field in the direction perpendicular to the slab surface with the inclusion of dipole corrections shown in Figure 1b. Specifically, we calculate the total energy of a clean Pt(100) surface and the adsorption energy of a water monomer on 2 × 2 supercells (i.e., 1/4 ML coverage level) with varying electric fields from −0.3 to 0.3 V/Å. The adsorption energy E_{ad} of a water monomer is calculated as

$$E_{\text{ad}}(\varepsilon) = E_{\text{H}_2\text{O/slab}}(\varepsilon) - E_{\text{slab}}(\varepsilon) - E_{\text{H}_2\text{O}} \quad (1)$$

where $E_{\text{H}_2\text{O/slab}}$ is the total energy of a Pt(100) slab with an adsorbed water, E_{slab} represents the energy of a clean Pt(100) slab, calculated with an electric field ε , and $E_{\text{H}_2\text{O}}$ is the energy of an isolated water molecule. Figure 2 shows that, on a Pt(100) surface, a water monomer preferentially adsorbs on the atop site for all strengths of the external electric fields considered. It can also be seen that the adsorption energy of a water monomer is influenced by the electric field and we observe an additional stabilization of the water monomer by about 0.15 eV. The response of any system to an electric field can be studied by expanding the energy as a function of the field strength as³¹

$$\Delta E(\varepsilon) = \mu\varepsilon - \frac{1}{2}\alpha_p\varepsilon^2 + \dots \quad (2)$$

where μ is the static dipole moment of system in the direction of the applied electric field and α_p denotes static polarizability.

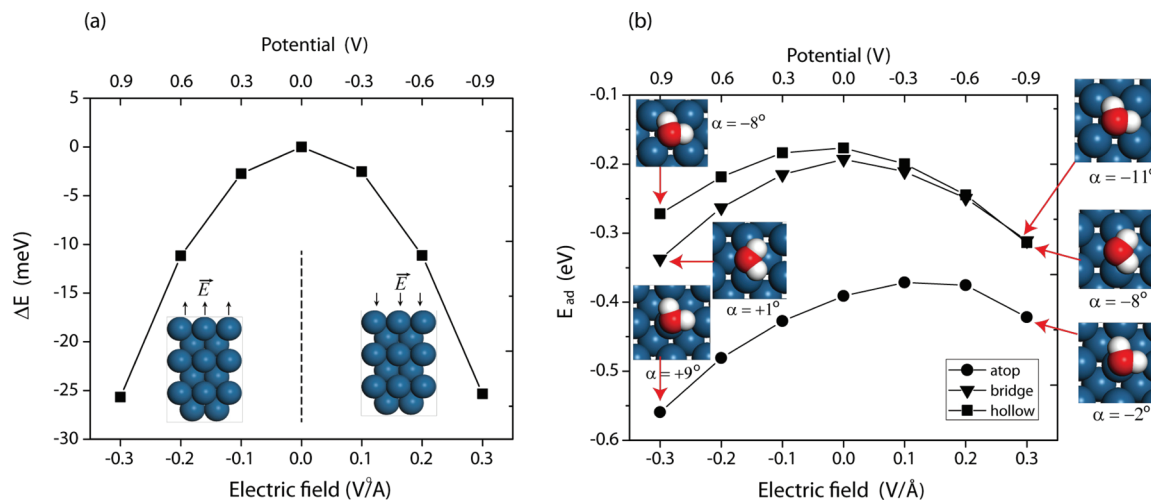


Figure 2. Ab initio calculated total energies as a function of external electric field of (a) clean Pt(100) surfaces, where total energies are normalized with respect to that at zero electric field, and (b) where a water monomer is adsorbed at a 2×2 supercell (1/4 ML coverage level). Structures of $\text{H}_2\text{O}/\text{Pt}(100)$ surfaces at -0.3 and 0.3 V/Å are inserted. The potentials are calculated assuming an electric double layer thickness of 3.0 Å.³¹

As the clean slab has inversion symmetry, the energy varies quadratically with the field strength, as shown in Figure 2a. However, in the case of $\text{H}_2\text{O}/\text{Pt}(100)$, the dipole moment of water adds a linear term in the expansion and a combined effect is observed in Figure 2b. The dipole moment of a isolated water molecule is about 0.39 eÅ, which amounts to about 0.12 eV stabilization at a field strength of -0.3 V/Å. Our results indicate that the adsorption energy changes are mostly due to the effect of water dipole moment. The angles between the water molecular plane and Pt(100) surface (denoted as α in Figure 2) show that an external electric field also slightly affects the direction of hydrogen atoms in water monomers adsorbed at atop and bridge sites. Since a negative electric field polarizes the Pt(100) surface by inducing positive charges, the stability of a water molecule with the hydrogen atom pointing away from the surface is higher than that of the configuration where the hydrogen points toward the surface. However, at hollow sites, hydrogen atoms always point down toward the Pt(100) surface regardless of the electric field, implying that there is an interaction with the Pt atoms located in the second layer directly below them. To summarize, the calculated results show that the overall effect of the electric field on the clean Pt(100) surface is marginal (~ 25 meV) but becomes significant when water adsorbs on the metal surface.

Table 1 shows the calculated adsorption energies and internal geometries of water monomers at various adsorption

incorporate the field effects, we explicitly apply an electric field of -0.3 V/Å in all calculations reported in this work.

Interfacial Water Structures. Moving from the computation of the preferential adsorption site to the computation of the stable water structure at the solid–liquid interface involves a search over the formidable configuration space introduced by the different possible atomic arrangements of Pt atoms and water molecules. We significantly reduce the computational cost of such a search using cluster expansion theory^{33–35} to parametrize atomic interaction energies between water molecules adsorbed on the Pt(100) surfaces. We have computed the total energies of 18 different $\text{H}_2\text{O}/\text{Pt}(100)$ surfaces as a function of water coverage (x) to obtain their formation energies, E_f defined as

$$E_f(x) = E_{\text{DFT}}(x) - E_0(x) \quad (3)$$

with

$$\begin{aligned} E_0(x) = & [E(\theta_{\text{H}_2\text{O}} = 1) - E(\theta_{\text{H}_2\text{O}} = 0)]x \\ & + E(\theta_{\text{H}_2\text{O}} = 0) \end{aligned} \quad (4)$$

where $E_0(x)$ is the energy of a weighted combination of a bare Pt(100) surface ($\theta_{\text{H}_2\text{O}} = 0$) and a H_2O monolayer ($\theta_{\text{H}_2\text{O}} = 1$) on the Pt(100) surface. $E_f(x)$ is a measure of the additional stability of the $\text{H}_2\text{O}/\text{Pt}(100)$ surface at coverage x relative to that of a homogeneous local environment at the same coverage x .

Before evaluating the interaction energies from cluster expansion, the relative chemical stabilities of the computed structures can be obtained from an energy convex hull mapped out from the formation energies of the computed structures, as shown in Figure 3. The energy convex hull shows the minimum energy configurations at different coverages, and a careful structural analysis of the two stable ground-state structures found at coverages of $2/3$ and $4/5$ ML indicates a general trend in the internal geometries of the adsorbed water molecules. Water molecules adsorb with two kinds of specific topologies, either with the molecular plane almost parallel, as shown in Figure 2 (here referred to as $\text{H}_2\text{O}(p)$) or with the molecular plane perpendicular to the surface (referred to as $\text{H}_2\text{O}(v)$).

The bond length between O and Pt atom of $\text{H}_2\text{O}(p)$ (~ 2.4 Å) is found to be much shorter than that in $\text{H}_2\text{O}(v)$ (~ 3.3 Å),

Table 1. Adsorption Energies and Internal Geometries of the Adsorbed Water Monomers at Different Sites Exposed to an External Electric Field of -0.3 V/Å

case	E_{ad} (eV)	$d_{\text{O}-\text{Pt}}$ (Å)	$d_{\text{O}-\text{H}}$ (Å)	$\angle(\text{HOH})$ (deg)
top	0.56	2.27	1.0	105.7
bridge	0.34	3.01	1.0	104.6
hollow	0.27	3.42	1.0	104.5

sites with an applied electric field of -0.3 V/Å. This field strength corresponds to an electrode potential of 0.9 V relative to the standard hydrogen electrode (SHE) using an electric double layer thickness of 3 Å.³¹ As seen from Table 1, the adsorption energy is well correlated with the bond distance $d_{\text{O}-\text{Pt}}$ which agrees well with previous findings.^{30–32} To

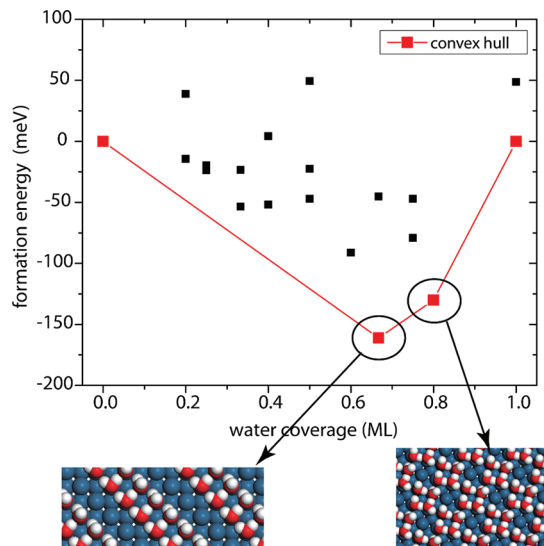


Figure 3. An ab initio calculated energy convex hull diagram of $\text{H}_2\text{O}/\text{Pt}(100)$ surfaces as a function of water coverage. Black and red squares denote the ab initio calculated 18 structures of different water coverage level, but only red squares indicate ground state structures. The detailed topologies of the ground structures at 2/3 and 4/5 ML were inserted below the energy convex hull diagram.

implying the adsorbed water forms the so-called bilayer structure often observed on $\text{Pt}(111)$ surfaces.^{31,36} However, the topology of the water bilayer is different from the hexagonal overlayer observed on (111) surfaces. The energy convex hull identifies two ground-state structures at intermediate coverage levels: They are (1×3) - $(\frac{1}{3}\text{H}_2\text{O}(\text{p}), \frac{1}{3}\text{H}_2\text{O}(\text{v}))$ and $(\sqrt{5} \times \sqrt{5})$ - $(\frac{2}{5}\text{H}_2\text{O}(\text{p}), \frac{2}{5}\text{H}_2\text{O}(\text{v}))$, according to Wood's notation,³⁷ and are shown in Figure 3. The morphologies of these structures are completely different. At lower coverages, water molecules order to form a zigzag shape of linear chain with two-thirds of the surface rows adsorbed by each of $\text{H}_2\text{O}(\text{p})$ and $\text{H}_2\text{O}(\text{v})$ and with the other row empty. As the surface coverage increases, the structure transforms into molecular rings with larger and smaller squared arrangements by water molecules. However, the formation energies of the two structures indicate that the (1×3) structure is more stable and there is a thermodynamic barrier for the phase transformation into the higher coverage structure.

Applying the cluster expansion methodology to the ab initio calculated formation energies leads to a parametrization of the molecular interaction energies among the two different adsorbed H_2O . Since the adsorbed water overlayer contains two distinct kinds of water molecules, two occupation variables are used, σ and δ , for $\text{H}_2\text{O}(\text{v})$ and $\text{H}_2\text{O}(\text{p})$, respectively, as shown in Figure 4. The formation energies are then expanded as functionals of these two occupation variables according to

$$\begin{aligned} E(\sigma, \delta) = & V_o + \sum_i^N V_i \sigma_i + \sum_j^N V_i \delta_i + \sum_{i,j}^N V_{i,j} \sigma_i \sigma_j \\ & + \sum_{i,j}^N V_{i,j} \sigma_i \delta_j + \sum_{i,j}^N V_{i,j} \delta_i \delta_j + \dots \end{aligned} \quad (5)$$

where the σ and δ are the mean cluster functionals composed of only $\text{H}_2\text{O}(\text{v})$ or $\text{H}_2\text{O}(\text{p})$, whereas the $\sigma\delta$ terms indicate coupled clusters with $\text{H}_2\text{O}(\text{p})$ and $\text{H}_2\text{O}(\text{v})$. The cluster

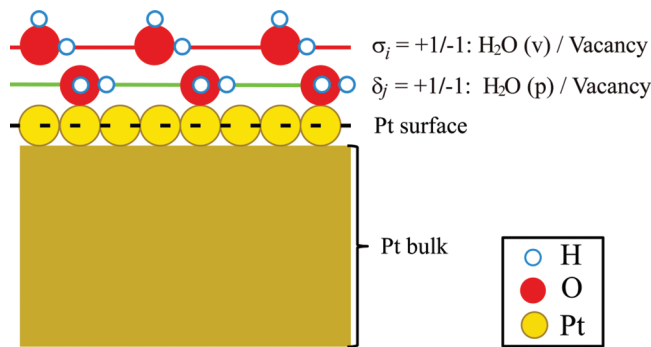


Figure 4. Side view of the model system for the cluster expansion of the $\text{H}_2\text{O}/\text{Pt}(100)$ surface. Two occupation variables are assigned for water adsorption sites: δ_j for $\text{H}_2\text{O}(\text{p})$ sites and σ_i for $\text{H}_2\text{O}(\text{v})$ sites.

expansion was optimized for the best fit to the formation energies with a minimal set of the truncation errors leading to a root-mean-square (rms) error of 13 meV and a cross validation score (CV) of 30 meV. The CV score is an indicator of the predictive energy resolution of the cluster expansion.³⁸ The optimum clusters and their effective cluster interaction (ECI) are illustrated in Figure 5.

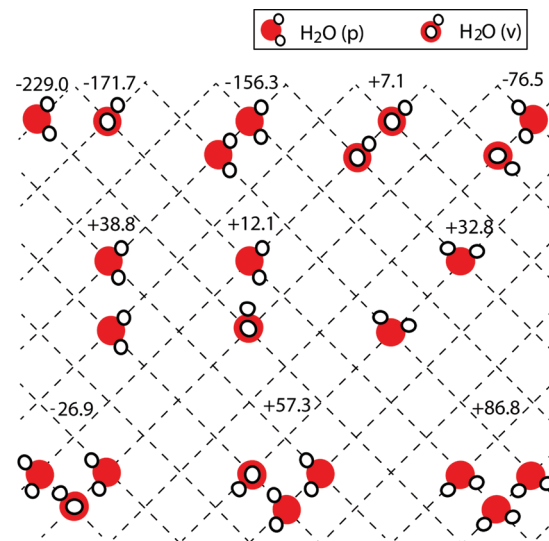


Figure 5. Optimized clusters and their ECI values (on the meV scale) in the cluster expansions for $\text{H}_2\text{O}/\text{Pt}(100)$ surfaces. Solid red (white) circles denote oxygen (hydrogen) atoms. The constant of the cluster expansion, V_o , is -185.74 meV. The cluster expansion characterizes the ECI value of each cluster; for example, the $V_{1,1}$ for the coupled cluster between the nearest neighbored $\text{H}_2\text{O}(\text{p})$ and $\text{H}_2\text{O}(\text{v})$ ($\sigma_1 \delta_1$) is -76.5 meV.

The ECI values of the individual clusters provide useful information about the nature of the complex adsorbate interactions involved. The high magnitude of nearest neighbor (NN), next-nearest neighbor (NNN), and three-body interactions shows that these are all important in determining the stable interfacial water structures. The ECIs of the point clusters show that $\text{H}_2\text{O}(\text{p})$ monomer adsorbs more strongly than $\text{H}_2\text{O}(\text{v})$ monomer. Considering the two-body, nearest neighbor interactions, $\text{H}_2\text{O}(\text{p})$ prefers $\text{H}_2\text{O}(\text{p})$ in its nearest neighbor environment. However, at the next-nearest neighbor distance, $\text{H}_2\text{O}(\text{p})$ repels $\text{H}_2\text{O}(\text{p})$. This shows that the addition of $\text{H}_2\text{O}(\text{p})$ to a nearest neighbor pair of $\text{H}_2\text{O}(\text{p})-\text{H}_2\text{O}(\text{p})$ is

energetically unfavorable. As a result, the triplets are only stable when $\text{H}_2\text{O}(\text{v})$ adsorbs with a pair of the nearest neighbor $\text{H}_2\text{O}(\text{p})$. The low CV score obtained shows that the expansion to next nearest neighbor distance and three-body is sufficient.

Using the parametrized interaction energies, Monte Carlo simulations were performed to identify the thermodynamically stable water structures as a function of the chemical potential of water, $\mu_{\text{H}_2\text{O}}$. Figure 6 shows that there is a sharp structural

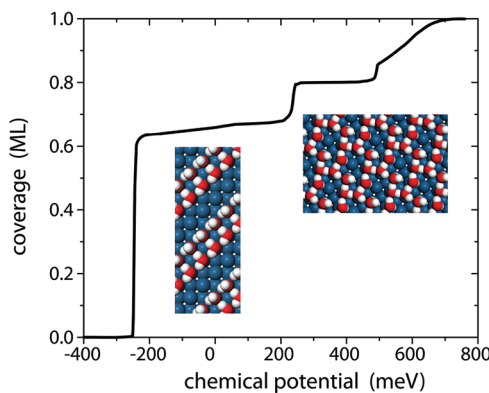


Figure 6. Monte Carlo simulations of the Pt(100) surface as a function of H_2O chemical potential at room temperature. Top views of the most stable interfacial water structures are inserted.

transition, from the clean (100) surface to the (1×3) ground structure approximately at $\mu_{\text{H}_2\text{O}} = -240$ meV, which is very close to the slope of the formation energy between the bare surface and the ground structure at $2/3$ coverage shown in Figure 3. This structure has chemical stability over a wide range of chemical potentials and continues to be stable until $\mu_{\text{H}_2\text{O}} = 200$ meV, where the higher coverage structure ($\sqrt{5} \times \sqrt{5}$) becomes the stable phase. This structure extends until $\mu_{\text{H}_2\text{O}} = 500$ meV. No other ordered phases are found until the surface is fully covered with water molecules, indicating the adsorbed water is in a disordered structure. It is to be noted that, although the rms error obtained from the cluster expansion is low, it is possible that more complicated interface structures (for, e.g., RT37 and RT39 seen in (111) surfaces) may be observed on (100) surfaces as well. However, in order to make the study computationally tractable, we have limited our

analysis to reasonably sized unit cells. Further, we use the interfacial water structure to study the water oxidation and other reactions relevant in electrochemical environments and we expect the trends to be similar for more complicated interface structures as well.

Water Oxidation. It has been observed on Pt(111) surfaces that, when the electrode potential increases, $\text{H}_2\text{O}(\text{v})$ oxidizes to form OH, which also forms hydrogen bonded networks with $\text{H}_2\text{O}(\text{p})$.⁷ To investigate water oxidation on Pt(100) surfaces, we have computed the formation energies of 50 different $(\text{H}_2\text{O}(\text{p})-\text{OH})/\text{Pt}(100)$ structures with varying coverage levels of OH and H_2O . A formation energy, $E_f(x,y)$, at a given coverage of x_{OH} and $y_{\text{H}_2\text{O}(\text{p})}$ can be defined as

$$E_f(x, y) = E_{\text{DFT}}(x, y) - E_0(x, y) \quad (6)$$

with

$$\begin{aligned} E_0(x, y) = & E(\theta_{\text{H}_2\text{O}(\text{p})} = 0, \theta_{\text{OH}} = 0) \\ & + [E(\theta_{\text{H}_2\text{O}(\text{p})} = 1, \theta_{\text{OH}} = 0) \\ & - E(\theta_{\text{H}_2\text{O}(\text{p})} = 0, \theta_{\text{OH}} = 0)]x \\ & + [E(\theta_{\text{H}_2\text{O}(\text{p})} = 0, \theta_{\text{OH}} = 1) \\ & - E(\theta_{\text{H}_2\text{O}(\text{p})} = 0, \theta_{\text{OH}} = 0)]y \end{aligned} \quad (7)$$

where $E_0(x,y)$ is the reference energy of Pt(100) surfaces with a weighted combination of x ML OH and y ML $\text{H}_2\text{O}(\text{p})$ without considering any interaction among the different phases. Figure 7 shows the energy convex hull of $(\text{H}_2\text{O}(\text{p})-\text{OH})/\text{Pt}(100)$ surfaces constructed by the ab initio calculated formation energies. The diagram suggests that the most viable path for the structural transition into an OH covered structure is first through the electrochemical oxidation of (1×3) - $(1/3\text{H}_2\text{O}(\text{p}), 1/3\text{H}_2\text{O}(\text{v}))$ into (1×3) - $(1/3\text{H}_2\text{O}(\text{p}), 1/3\text{OH})$. The diagram also suggests that this could be followed by a further transformation into a fully covered (1×2) - $(1/2\text{H}_2\text{O}(\text{p}), 1/2\text{OH})$ structure. Although $(1/5\text{H}_2\text{O}(\text{p}), 4/5\text{OH})$ and $(2/3\text{H}_2\text{O}(\text{p}), 1/3\text{OH})$ are stable structures, these structures do not share a Gibbs triangle with (1×3) - $(1/3\text{H}_2\text{O}(\text{p}), 1/3\text{OH})$. This makes the routes of these phase transitions thermodynamically unfavorable.

To obtain the molecular interaction energies between the H_2O and OH, a cluster expansion was carried out for the

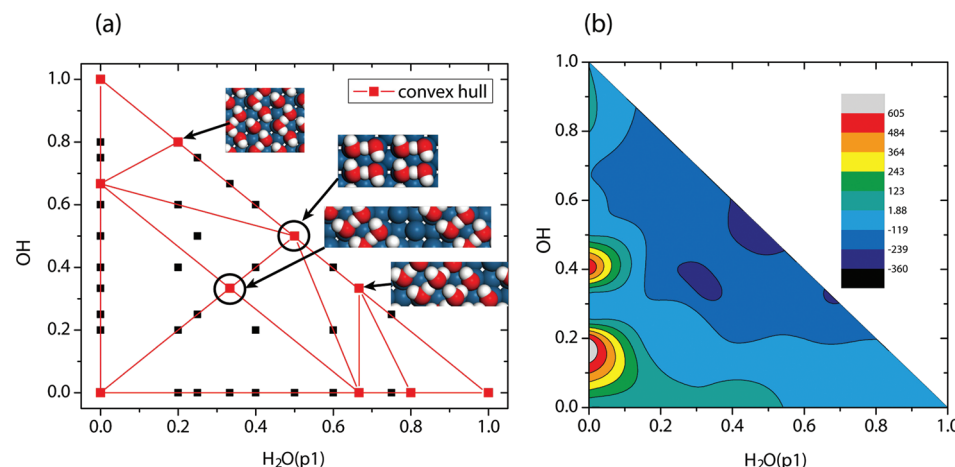


Figure 7. (a) Ab initio calculated energy convex hull of OH- $\text{H}_2\text{O}/\text{Pt}(100)$ surfaces; (b) the contour plot of the convex hull.

formation energies of all computed configurations using two occupation variables for $\text{H}_2\text{O}(\text{p})$ and OH, respectively, similar to that done earlier. Error minimization of the expansion enables the identification of the optimum clusters and ECIs. We find an rms error of 27 meV and a CV score of 41 meV using the optimum clusters shown in Figure 8. The ECIs show that

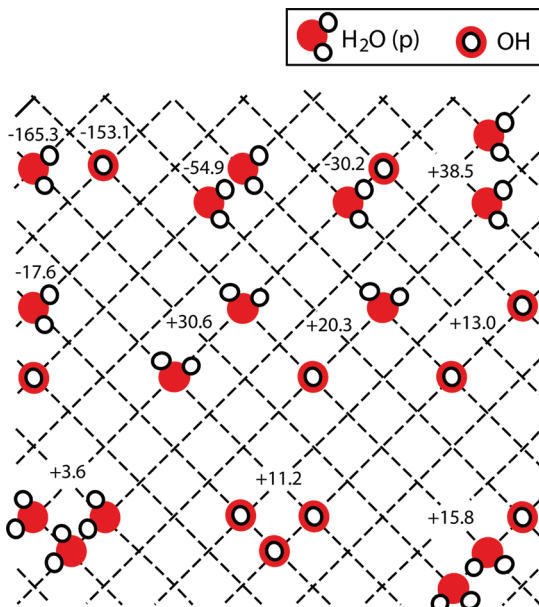
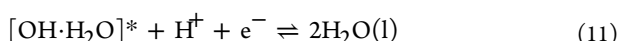
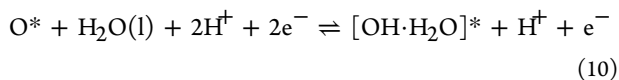
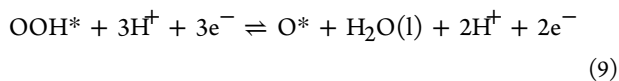
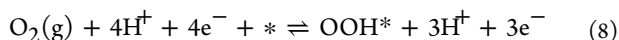


Figure 8. Optimized clusters and ECIs identified by the cluster expansion of the ab initio calculated formation energies. The constant of the cluster expansion is $V_0 = -183.8 \text{ meV}$.

OH and $\text{H}_2\text{O}(\text{p})$ adsorb with similar adsorption energies on the Pt(100) surfaces. Although the $\text{H}_2\text{O}(\text{p})-\text{H}_2\text{O}(\text{p})$ pair has the most attractive nearest neighbor interaction, at the next-nearest neighbor distance, the $\text{H}_2\text{O}(\text{p})-\text{H}_2\text{O}(\text{p})$ interaction is repulsive, while the $\text{H}_2\text{O}(\text{p})-\text{OH}$ interaction is attractive. This implies that the overall chemical attraction between OH and $\text{H}_2\text{O}(\text{p})$ is stronger than between a pair of $\text{H}_2\text{O}(\text{p})$. Three-body clusters composed of all water or OH groups and linear combinations of the two species all repel, although the magnitudes of ECIs are smaller than the pair clusters. These subtle interactions lead to stabilization of the (1×2) - $(\frac{1}{2}\text{H}_2\text{O}(\text{p}), \frac{1}{2}\text{OH})$ structure depicted in Figure 7.

Oxygen Reduction Reaction. In addition to the stable interfacial water structure and the water-hydroxyl structure, there are two additional intermediates relevant for oxygen reduction reaction, namely, O^* and OOH^* . We follow the same mechanism for oxygen reduction reaction as that used for Pt(111) in an earlier work.³⁹



where $*$ means a clean Pt(100) surface site available for adsorption. The reversible potentials (U°) of the four reactions are calculated as

$$U_1^\circ = \Delta G_{\text{O}_2} + \frac{1}{2}\Delta G_{\text{H}_2} - \Delta G_{\text{OOH}^*} - \Delta G_{\text{corr},\text{OOH}^*} \quad (12)$$

$$U_2^\circ = \Delta G_{\text{OOH}^*} + \Delta G_{\text{corr},\text{OOH}^*} + \frac{1}{2}\Delta G_{\text{H}_2} - \Delta G_{\text{O}^*} - \Delta G_{\text{corr},\text{O}^*} - \Delta G_{\text{H}_2\text{O}(\text{l})} \quad (13)$$

$$U_3^\circ = \Delta G_{\text{O}^*} + \Delta G_{\text{corr},\text{O}^*} + \Delta G_{\text{H}_2\text{O}(\text{l})} + \frac{1}{2}\Delta G_{\text{H}_2} - \Delta G_{\text{OH}-\text{H}_2\text{O}^*} \quad (14)$$

$$U_4^\circ = \Delta G_{\text{OH}-\text{H}_2\text{O}^*} + \frac{1}{2}\Delta G_{\text{H}_2} - 2\Delta G_{\text{H}_2\text{O}(\text{l})} \quad (15)$$

where ΔG_i is the ab initio calculated free energy for intermediate i , which is obtained by including the differences in total internal energies, zero-point energy, and entropy. ΔG_{corr} is the free energy correction for the different intermediates, as shown in Table 2. Specifically, $\Delta G_{\text{corr},\text{OOH}^*}$ is due

Table 2. Free Energy Corrections

free energy	description	correction (eV)
$\Delta G_{\text{corr},\text{OOH}^*}$	stabilization energy of adsorbed OOH	-0.31: $(1 \times 3) \rightarrow (2 \times 6)$ supercells
$\Delta G_{\text{corr},\text{O}^*}$	stabilization energy of adsorbed O	-0.42: $(1 \times 3) \rightarrow (2 \times 2)$ supercells

to an additional chemical stabilization of the intermediate OOH surrounded with H_2O and OH. We estimate the free energy correction by calculating a formation energy of adsorbed OOH using (2×6) cells with three OH and four H_2O in its neighbor environment. $\Delta G_{\text{corr},\text{O}^*}$ compensates for the chemical stability of adsorbed oxygen atom induced by a structural transformation from (1×3) to (2×2) cells. We use the zero-point vibrational energies and entropic corrections as those used by Hansen et al.³⁹

The resulting reversible potentials are shown in Table 3 along with the reversible potentials for oxygen reduction reaction on the Pt(111) surface using a hexagonal water overlayer for comparison. The calculated reversible potentials for (111) agree well with those reported in earlier work.^{30,31,39} As can be seen from Table 3, we find that OOH^* binds stronger on the (100) facet than on (111) surfaces as would be expected. The potential limiting step on Pt(100) is also the reduction of OH^* to water. However, due to a much stronger binding of OH^* intermediate on the Pt(100) surface, the thermodynamic limiting overpotential is higher than that on Pt(111).

It is to be noted that, in a recent work, Tian and Anderson have studied the effective reversible potentials for the formation of different intermediates for ORR.⁴⁰ They report that the formation of OOH^* from adsorbed O_2 in the environment of coadsorbed H_2O molecules on the Pt(111) surface at around 0.4 V. This is different from that reported in this work as well that of Hansen et al., and this is likely caused by a different choice of the reference state of O_2 . We have chosen the reference state to be O_2 gas obtained from the H_2O reference as outlined in earlier works.^{30,39}

Using the reversible potentials, we show the free energy diagram for ORR on the Pt(100) surface as a function of the

Table 3. Ab Initio Calculated Reversible Potentials of ORR on Pt(111) and Pt(100) Surfaces^a

reaction	Pt(111)	Pt(100)
$O_2(g) + 4H^+ + 4e^- + * \rightleftharpoons OOH^* + 3H^+ + 3e^-$	0.78	0.88
$OOH^* + 3H^+ + 3e^- \rightleftharpoons O^* + H_2O(l) + 2H^+ + 2e^-$	2.48	2.31
$O^* + H_2O + 2H^+ + 2e^- \rightleftharpoons [OH\cdot H_2O]^* + H^+ + 2e^-$	0.90	1.19
$[OH\cdot H_2O]^* + H^+ + 2e^- \rightleftharpoons 2H_2O$	0.75	0.54

^aWe have provided the calculated reversible potentials on Pt(111) surfaces for comparison.

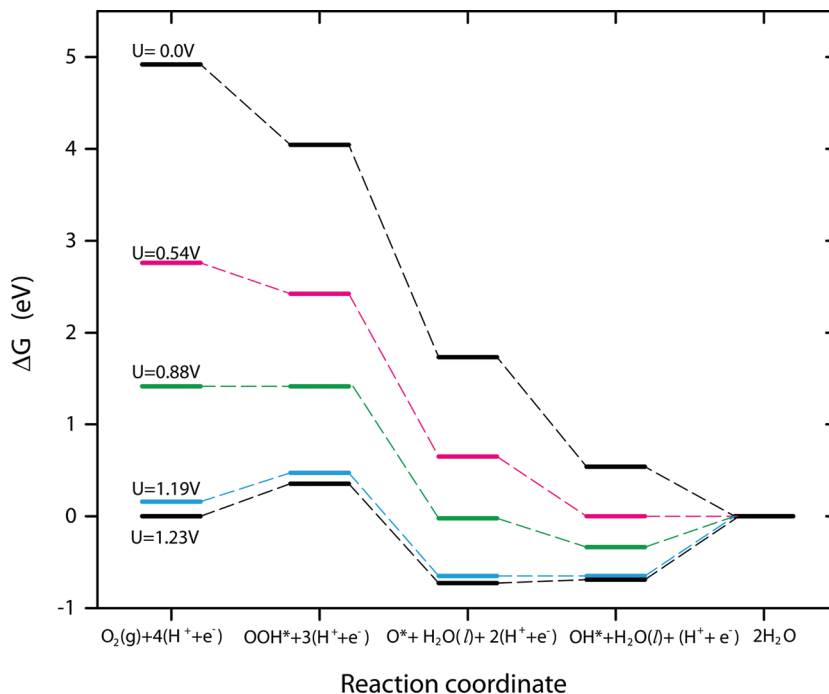


Figure 9. Free energy diagram of intermediates in ORR on the Pt(100) surfaces as a function of the electrode potential.

electrode potential (U) in Figure 9. We include the effect of potential on all the intermediates by shifting the free energy of the electron by $-neU$, where U is the electrode potential and n is the number of electrons involved. The figure shows that, compared to Pt(111), Pt(100) surface more easily activate OOH^* ; however, they also bind O^* and OH^* stronger. The large drop in energy of reaction 9 is consistent with the discussion of Tian and Anderson,⁴⁰ who point out that one of the major limitations of activity at higher potentials is the chemical dissociation of OOH , which is here lumped with the reduction of OH into this reaction 9. The limiting potential where all of the steps remain downhill is at $U = 0.54$ V, beyond which the reduction of OH^* to water becomes thermodynamically uphill. This limiting thermodynamic potential of $U = 0.54$ V is much smaller than that on the Pt(111) surface, where the reaction is thermodynamically downhill up to a potential of $U = 0.75$ V. This is consistent with experimental evidence for the lower activity of the (100) facets in comparison to the (111) facets in a nonadsorbing electrolyte such as $HClO_4$.^{41,42}

Comparison to Experiment. In this section, using the calculated thermodynamics of different intermediates in the earlier section, we make direct comparisons to voltammetric and rotating ring disk electrode experiments to evaluate the electrochemical activity of the Pt(100) surface for oxygen reduction reaction.

Surface Structure. Before comparisons of the model can be made to experiments, it is to be noted that the Pt(100) surface when prepared in UHV by sputtering and annealing reconstructs into a hexagonal, densely packed form.¹⁵ Recent STM imaging of the Pt(100) surface shows that, in contact with electrolytes, the Pt(100)-hex surface, that was prepared either in UHV or by a flame annealing method,¹⁶ is lifted and becomes a (1×1) surface with a lot of defects.¹⁶ The defect sites are expected to bind O intermediates strongly and thus are likely inactive, and we would expect the activity to be dominated by the Pt(100)- (1×1) surface sites. This gives confidence in comparing the results of the developed model for the unreconstructed Pt(100) surface to voltammetric and rotating ring disk electrode experiments.

Cyclic Voltammetry. Here, we use the computed reversible potentials to determine the potential dependence of O and OH adsorption, which can be examined experimentally by cyclic voltammetry in an O_2 free environment such as N_2 . The water discharge reactions, i.e., the oxidation of H_2O to OH and O (reactions 10 and 11 shown above), are typically in dynamic equilibrium,⁴³ thus providing a way to validate the computed reversible potentials for these reactions by benchmarking against voltammetric measurements on the Pt(100) surface.

The coverage of O-containing species is obtained by integrating a linear sweep voltammogram from the potential of zero charge while correcting for the double-layer capacitance.

The precise experimental quantification of O-containing adsorbates is rather difficult for Pt(100) compared to Pt(111) surface, as there is a significant overlap existing between the hydrogen and the OH adsorption regions.^{7,44,45} This overlap makes the direct determination of the maximum OH coverage from the integration of the voltammetric current density difficult. Feliu et al.⁴⁴ have used a deconvolution analysis where they have estimated the value of maximum charge density associated with the adsorption of hydroxyl species. This information has been obtained from charge displacement experiments by integrating the cyclic voltammetry from the potential of zero charge, which is 0.43 V for Pt(100) in contact with 0.1 M HClO₄ at room temperature,⁴⁶ up to a more positive potential where the voltammetric current (corrected for the double-layer contribution) goes to zero. Using this deconvolution, a value of 77 μC/cm² is obtained, which should correspond to the maximum charge density due to the adsorption of hydroxyl species. This corresponds to a maximum value of 0.37 OH species per surface platinum atom.⁴⁴ In addition, they also observe that this maximum saturation coverage is independent of temperature within the accuracy of the experimental technique.

Figure 10 shows the surface coverages of O and OH on Pt(100) surfaces calculated by dynamic Monte Carlo (DMC)

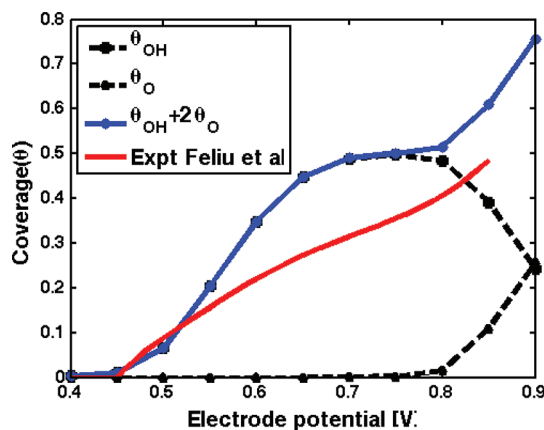


Figure 10. Coverage of O-containing adsorbates on the Pt(100) surface as a function of electrode potential. Experimental results were taken from the work of Feliu et al.⁴⁴

simulations using the DFT-calculated interaction energies and reversible potentials under dynamic equilibrium. We use a simple Butler–Volmer formulation for the rates of the electrochemical reactions, given by $k_i^0 \exp(-\alpha F(U - U_0)/RT)$ using $\alpha = 0.5$, where U_0 is the reversible potential of the considered electrochemical reaction. We note that these electrochemical reactions are assumed to be in dynamic equilibrium, and thus, we compare the equilibrium coverages obtained from the DMC simulations to the experiments. The onset of OH adsorption is observed around 500 mV, which matches the experimental onset. The simulations show the formation of a $^{1/3}\text{OH}$ phase at 600 mV, which subsequently undergoes a phase transformation into a $^{1/2}\text{OH}$ phase. However, here we note that there is a deviation in the saturation coverages observed in the results of our model and the experiment.⁴⁴ This could be due to the limitations of the model, as it is, in principle, possible for OH–H₂O structures to have a different local structure. In addition, as seen in STM images,¹⁶ the (1 × 1)-(100) surface contains a lot of defects

which could affect the saturation coverage. In the potential window between 600 and 700 mV, the OH coverage reaches a plateau, similar to the behavior seen in the experiments. Further oxidation happens beyond 800 mV, which in our model is attributed to the oxidation of OH to O. However, at these potentials, bulk or subsurface oxidation might also occur, which is beyond the scope of this study.⁴⁷

Rotating Ring Disk Electrode Experiment. Here, we use a simple model to determine the oxygen reduction reaction polarization curves to compare against rotating ring disk electrode experiments. The model uses the fact that there is a difference of the electrochemical prefactors involving the reactions of the water discharge (reactions 10 and 11) and the first reduction step of oxygen (reaction 8). In the case of the reaction involving the oxidation of water, the prefactor depends on the water concentration. However, in the case of the first reduction step, the prefactor is determined by the dissolved oxygen concentration at the interface. A simple estimate by Henry's law yields a ratio of 10⁵ for the ratio of the water concentration to the oxygen concentration. As a result, we expect the reactions involving the water discharge reaction to be in dynamic equilibrium, which then determine the equilibrium coverage of O and OH. This is further validated by the fact that the coverage of O and OH species is nearly the same in N₂ purged and O₂ purged environments, showing that there is no significant build up of O and OH from the reduction of O₂.⁴⁸ Thus, the current density will be determined by a combination of the rate of the first reduction step of oxygen in addition to the free sites available, which is governed by the water discharge reaction. This is similar to the approach used by Rossmeisl et al.⁴⁹ It is to be noted that a similar argument holds for basic electrolytes as well, since the adsorbed intermediates along the reaction coordinate are independent of the concentration of protons.³⁹ The main difference for basic environment is the chemical potential of the protons and that the proton donor changes from being a hydronium ion in acid electrolytes to being H₂O in alkaline electrolytes.

The comparison to the experimental results of Macia et al.⁴² is carried out by calculating the total current, including the diffusion limited current. This is calculated using the relation

$$\frac{1}{j} = \frac{1}{j_D} + \frac{1}{j_k} \quad (16)$$

where j is the total current density, j_D is the measured diffusion limited current density, and j_k is the calculated kinetic current density from the DMC simulations. A value of $j_D = -6.0 \text{ mA/cm}^2$ was used to make the comparison from the model to that of the experiments.

Figure 11 shows the simulated polarization curve using the calculated reversible potentials and a comparison with the experimental results of Macia et al.⁴² We find a reasonable agreement between the results of the model and the experimental polarization measurements. At potentials below 600 mV, there are no kinetic limitations and the total current is limited by mass transport. At potentials beyond 600 mV, the surface starts to get poisoned by OH. It is to be noted that at this potential all of the other steps are thermodynamically downhill. Therefore, the current is being limited by the reduction of OH to H₂O. At higher potentials beyond 700 mV, a mixed effect of site blocking due to OH and the activation of OOOH is observed. The half-wave potential obtained from our model is around 700 mV, which shows a 100 mV deviation

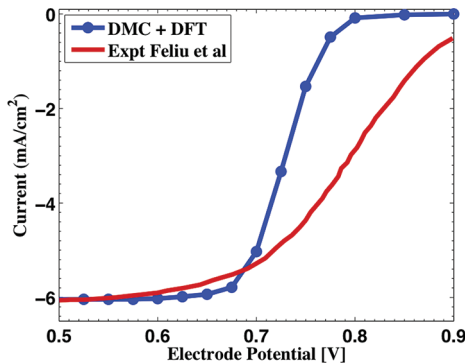


Figure 11. Polarization curves for oxygen reduction reaction. The experimental data is taken from the work of Macia et al.⁴²

from that seen in the experiments. In this work, we have used a simple model to calculate the polarization curve using the calculated reversible potentials. It is to be noted that there might be other kinetic barriers and additional effects of water stabilization on the intermediates.

Comparison between (111) and (100) Facets. The results of our model show that the interaction of the Pt(100) surface with the interfacial water layer is more complex than that for Pt(111). Because of the geometric mismatch, it is found that both multibody and long-range interactions are energetically important and need to be considered. It is also found that the Pt(100) surfaces bind oxygen intermediates, O and OH, stronger than the Pt(111) surface, as would be expected from the coordination number of the surface metal atoms. This makes it difficult to remove especially OH in the reduction step to water. We also have shown that the limiting thermodynamic potential, defined as the potential where all of the steps are downhill in free energy, is much lower on Pt(100) (0.54 V) than that on Pt(111) (0.75 V). As a result, at the fuel cell operating voltage of around 0.7–0.8 V, we would expect the activity of Pt nanoparticles to be dominated by the (111) facet.

■ CONCLUSION

We have calculated the thermodynamically stable interfacial water structure on Pt(100) surfaces by combining cluster expansion theory and Monte Carlo simulations. It is found that multibody and long-range interaction potentials of water molecules as well as the lattice topology of Pt surfaces are important factors, which have to be considered for an accurate prediction of the adlayer structure. Our results indicate that, for ORR, because of enhanced OH poisoning, unreconstructed Pt(100) surfaces are much less catalytically active than Pt(111) planes.

■ AUTHOR INFORMATION

Corresponding Author

*E-mail: hanbc@dgist.ac.kr (B.H.); h.pitsch@stanford.edu (H.P.). Phone: +1 650 736 1995. Fax: +1 650 725 3525.

Notes

The authors declare no competing financial interest.

■ ACKNOWLEDGMENTS

This research work was supported by Honda Research Center in Japan and NSF grant award number 0644470. This work was also supported in part by DGIST through award number 11-BD-0405. V.V. gratefully acknowledges support from The

Electrochemical Society Herbert H Uhlig Summer Fellowship and United Technologies Fellowship. The authors would like to thank Dr. Heine Hansen for helpful discussions.

■ REFERENCES

- (1) Thiel, P. A.; Maday, T. E. *Surf. Sci. Rep.* **1987**, *7*, 211–385.
- (2) Henderson, M. A. *Surf. Sci. Rep.* **2002**, *46*, 1–308.
- (3) Hodgson, A.; Haq, S. *Surf. Sci. Rep.* **2009**, *64*, 381–451.
- (4) Feibelman, P. J. *Science* **2002**, *295*, 99–102.
- (5) Morgenstern, M.; Michely, T.; Comsa, G. *Phys. Rev. Lett.* **1996**, *77*, 703–706.
- (6) Meng, S.; Wang, E. G.; Gao, S. *Phys. Rev. B* **2004**, *69*, 195404.
- (7) Garcia-Araez, N.; Climent, V.; Feliu, J. *J. Phys. Chem. C* **2009**, *113*, 9290–9304.
- (8) Seong, S.; Anderson, A. B. *J. Phys. Chem.* **1996**, *100*, 11744–11747.
- (9) Tang, L.; Han, B. C.; Persson, K.; Friesen, C.; He, T.; Sieradzki, K.; Ceder, G. *J. Am. Chem. Soc.* **2010**, *132*, 596–600.
- (10) Ball, S. C.; Hudson, S. L.; Leung, J. H.; Russell, A. E.; Thompsett, D.; Theobald, B. R. *ECS Trans.* **2007**, *11*, 1247–1257.
- (11) Stamenkovic, V. R.; Mun, B. S.; Arenz, M.; Mayrhofer, K. J. J.; Lucas, G.; Wang, C. A.; Ross, P.; N. Markovic, N. M. *Nat. Mater.* **2007**, *6*, 241–247.
- (12) Xiong, Y.; Wiley, B.; Xia, Y. *Angew. Chem., Int. Ed.* **2007**, *46*, 7157.
- (13) Hammer, B.; Nørskov, J. *Adv. Catal.* **2000**, *45*, 71–129.
- (14) Nørskov, J. K.; Rossmeisl, J.; Logadottir, A.; Lindqvist, L.; Kitchin, J. R.; Bligaard, T.; Jonsson, H. *J. Phys. Chem. B* **2004**, *108*, 17886–17892.
- (15) Kolb, D. *Prog. Surf. Sci.* **1996**, *51*, 109–173.
- (16) Strmcnik, D. S.; Tripkovic, D. V.; van der Vliet, D.; Chang, K.-C.; Komanicky, V.; You, H.; Karapetrov, G.; Greeley, J.; Stamenkovic, V. R.; Marković, N. M. *J. Am. Chem. Soc.* **2008**, *130*, 15332–15339.
- (17) Greeley, J.; Rossmeisl, J.; Hellman, A.; Nørskov, J. K. *Z. Phys. Chem.* **2007**, *221*, 1209–1220.
- (18) Rai, V.; Aryanpour, M.; Pitsch, H. *J. Phys. Chem. C* **2008**, *112*, 9760–9768.
- (19) Viswanathan, V.; Hansen, H.; Rossmeisl, J.; Jaramillo, T.; Pitsch, H.; Nørskov, J. K. *J. Phys. Chem. C* **2012**, *116*, 4698–4704.
- (20) Blöchl, P. E. *Phys. Rev. B* **1994**, *50*, 17953–17979.
- (21) Perdew, J. P.; Burke, K.; Ernzerhof, M. *Phys. Rev. Lett.* **1996**, *77*, 3865–3868.
- (22) Kresse, G.; Furthmuller, J. *Comput. Mater. Sci.* **1996**, *6*, 15–50.
- (23) Methfessel, M.; Paxton, A. T. *Phys. Rev. B* **1989**, *40*, 3616–3621.
- (24) Lide, D. R., Ed. *CRC Handbook of Chemistry and Physics*; CRC: New York, 1996.
- (25) Gillespie, D. T. *J. Comput. Phys.* **1976**, *22*, 403–434.
- (26) Lukkien, J. J.; Segers, J. P. L.; Hilbers, P. A. J.; Gelten, R. J.; Jansen, A. P. *J. Phys. Rev. E* **1998**, *58*, 2598–2610.
- (27) Reese, J. S.; Raimondeau, S.; Vlachos, D. G. *J. Comput. Phys.* **2001**, *173*, 302–321.
- (28) Rai, V.; Pitsch, H.; Novikov, A. *Phys. Rev. E* **2006**, *74*, 046707.
- (29) Viswanathan, V.; Wang, F.; Pitsch, H. *Comput. Sci. Eng.* **2012**, *14* (2), 60–68.
- (30) Karlberg, G. S.; Rossmeisl, J.; Nørskov, J. K. *Phys. Chem. Chem. Phys.* **2007**, *9*, 5158–5161.
- (31) Rossmeisl, J.; Nørskov, J. K.; Taylor, C. D.; Janik, M. J.; Neurock, M. *J. Phys. Chem. B* **2006**, *110*, 21833–21839.
- (32) Blanco, R.; Orts, J. M. *Electrochim. Acta* **2008**, *53*, 7796–7804.
- (33) Han, B. C.; Van der Ven, A.; Ceder, G.; Hwang, B. *J. Phys. Rev. B* **2005**, *72*, 205409.
- (34) Fontaine, D. D. *Solid State Phys.* **1994**, *47*, 33–176.
- (35) Sanchez, J. M. *Phys. Rev. B* **2010**, *81*, 224202.
- (36) Ogasawara, H.; Brena, B.; Nordlund, D.; Nyberg, M.; Pelmenschikov, A.; Pettersson, L. G. M.; Nilsson, A. *Phys. Rev. Lett.* **2002**, *89*, 276102.
- (37) Wood, E. *J. Appl. Phys.* **1964**, *35*, 1306–1312.
- (38) van de Walle, A.; Ceder, G. *J. Phase Equilibr.* **2002**, *23*, 348–359.

- (39) Hansen, H. A.; Rossmeisl, J.; Nørskov, J. K. *Phys. Chem. Chem. Phys.* **2008**, *10*, 3722–3730.
- (40) Tian, F.; Anderson, A. B. *J. Phys. Chem. C* **2011**, *115*, 4076–4088.
- (41) Markovic, N. M.; Ross, P. N. *Surf. Sci. Rep.* **2002**, *45*, 117–229.
- (42) Macia, M.; Campina, J.; Herrero, E.; Feliu, J. M. *J. Electroanal. Chem.* **2004**, *564*, 141–150.
- (43) Wang, J. X.; Markovic, N. M.; Adzic, R. R. *J. Phys. Chem. B* **2004**, *108*, 4127–4133.
- (44) Climent, V.; Gomez, R.; Orts, J. M.; Feliu, J. M. *J. Phys. Chem. B* **2006**, *110*, 11344–11351.
- (45) Garcia-Araez, N. *J. Phys. Chem. C* **2011**, *115*, 501–510.
- (46) Gómez, R.; Orts, J.; Alvarez-Ruiz, B.; Feliu, J. *J. Phys. Chem. B* **2004**, *108*, 228–238.
- (47) Tang, L.; Han, B.; Persson, K.; Friesen, C.; He, T.; Sieradzki, K.; Ceder, G. *J. Am. Chem. Soc.* **2010**, *132*, 596–600.
- (48) Bondarenko, A. S.; Stephens, I. E. L.; Hansen, H. A.; Pérez-Alonso, F. J.; Tripkovic, V.; Johansson, T. P.; Rossmeisl, J.; Nørskov, J. K.; Chorkendorff, I. *Langmuir* **2011**, *27*, 2058–2066.
- (49) Rossmeisl, J.; Karlberg, G. S.; Jaramillo, T.; Nørskov, J. K. *Faraday Discuss.* **2009**, *140*, 337–346.